

Reducing the Object Orientation Dependence of Susceptibility Effects in Gradient Echo MRI Through Quantitative Susceptibility Mapping

Jianqi Li,¹ Shixin Chang,² Tian Liu,^{3,4} Qianfeng Wang,¹ Deqi Cui,⁵ Xiaoyue Chen,³ Moonsoo Jin,³ Baocheng Wang,⁶ Mengchao Pei,¹ Cynthia Wisnieff,^{3,4} Pascal Spincemalle,⁴ Min Zhang,¹ and Yi Wang^{1,3,4,7*}

This study demonstrates the dependence of non-local susceptibility effects on object orientation in gradient echo MRI and the reduction of non-local effects by deconvolution using quantitative susceptibility mapping. Imaging experiments were performed on a 3T MRI system using a spoiled 3D multi-echo GRE sequence on phantoms of known susceptibilities, and on human brains of healthy subjects and patients with intracerebral hemorrhages. Magnetic field measurements were determined from multiple echo phase data. To determine the quantitative susceptibility mapping, these field measurements were deconvolved through a dipole inversion kernel under a constraint of consistency with the magnitude images. Phantom and human data demonstrated that the hypointense region in GRE magnitude image corresponding to a susceptibility source increased in volume with TE and varied with the source orientation. The induced magnetic field extended beyond the susceptibility source and varied with its orientation. In quantitative susceptibility mapping, these blooming artifacts, including their dependence on object orientation, were reduced, and the material susceptibilities were quantified. Magn Reson Med 000:000–000, 2011. © 2011 Wiley Periodicals, Inc.

Key words: gradient echo; blooming artifacts; quantitative susceptibility mapping; hemorrhage

The gradient-recalled-echo (GRE) sequence is a fundamental pulse sequence in magnetic resonance imaging (MRI) (1) and is routinely used in clinical practice and scientific research for applications including three-

dimensional (3D) high-resolution anatomy, dynamic contrast enhanced MRI, magnetic resonance angiography, tissue perfusion, and functional MRI (2). A distinct feature of GRE is its sensitivity to tissue magnetic susceptibility. Tissue becomes magnetized in the MRI scanner and generates an inhomogeneous magnetic field that contributes to spin phase during GRE signal detection. Phase dispersion within a voxel leads to the well-known T_2^* hypointensity, which can be attenuated further retrospectively by a phase mask to produce susceptibility weighted imaging (SWI) (3–5). These susceptibility effects on MR signal magnitude and phase are very important for tissue characterization in high-field MRI, particularly in 7T brain imaging (6,7). It is well known that imaging parameters including main field strength, echo time (TE), and voxel size affect these susceptibility artifacts in GRE MRI, which can be a serious challenge in clinical applications (8–10).

A major difficulty in interpreting GRE is that the susceptibility effect is non-local, i.e., susceptibility effects within a voxel arise not only from sources within that voxel but also from neighboring sources outside that voxel. The induced magnetic field extends beyond the susceptibility source in a dipole field pattern according to the Maxwell's Equations, the law of magnetism. The GRE signal at a location may still have a non-zero phase due to the presence of nearby susceptibility sources even though there is no significant source of susceptibility in that location. Therefore, T_2^* hypointensity and phase contrast in GRE are not directly reflective of local tissue properties (11). A dipole deconvolution of the measured magnetic field is required to generate quantitative susceptibility maps (QSM) of local tissues (12–23).

Recently, there has been increasing interest in the biophysical interpretation of the orientation-dependence of susceptibility effects of fibers (24–26) and macrostructures (27). In this paper, we use the Maxwell's Equations to investigate the object orientation dependence of the blooming artifacts in GRE magnitude and phase images, and we use QSM to reduce the orientation dependent blooming artifacts.

MATERIALS AND METHODS

GRE MRI experiments were performed on phantoms with known susceptibility distributions, healthy human subjects, and patients with intracerebral hemorrhages. A

¹Shanghai Key Laboratory of Magnetic Resonance and Department of Physics, East China Normal University, Shanghai, China.

²Department of Radiology, Yueyang Hospital of Integrated Traditional Chinese and Western Medicine, Shanghai University of Traditional Chinese Medicine, Shanghai, China.

³Department of Biomedical Engineering, Cornell University, Ithaca, New York, USA.

⁴Department of Radiology, Weill Medical College of Cornell University, New York, New York, USA.

⁵School of Optoelectronics, Beijing Institute of Technology, Beijing, China.

⁶Department of Neurosurgery, Yueyang Hospital of Integrated Traditional Chinese and Western Medicine, Shanghai University of Traditional Chinese Medicine, Shanghai, China.

⁷Department of Biomedical Engineering, Kyung Hee University, Seoul, Korea. Grant sponsor: Science and Technology Commission of Shanghai Municipality, China; Grant number: 10JC1414600; Grant sponsor: NIH; Grant number: 1R01EB013443.

*Correspondence to: Yi Wang, PhD, 416 E 55th Street, New York, NY, 10022. E-mail: yiwang@med.cornell.edu

Received 29 August 2011; revised 8 November 2011; accepted 4 December 2011.

DOI 10.1002/mrm.24135

Published online in Wiley Online Library (wileyonlinelibrary.com).

© 2011 Wiley Periodicals, Inc.

Table 1
3D GRE Image Parameters for Iron Oxide Phantoms and Human Subjects

	Phantom #1	Phantom #2	Human subjects
Reception coil	32-channel head coil	4-channel animal coil	12-channel head coil
Imaging plane	Coronal	Coronal	Sagittal
Repetition time (ms)	40	40	30
No. of echoes	9	8	8
1st echo time (ms)	4.0	4.2	3.3
Echo spacing (ms)	4.0	4.2	3.3
Flip angle (degrees)	15	15	15
Field of view (mm)	150 × 150	77 × 77	240 × 240
Slice thickness (mm)	1.2	0.6	1.25
Matrix	128 × 128 × 64	128 × 128 × 128	192 × 192 × 128
Signal average	4	2	1
Voxel size (mm ³)	1.2 × 1.2 × 1.2	0.6 × 0.6 × 0.6	1.25 × 1.25 × 1.25

convolution with the magnetic field of a unit dipole (the dipole kernel) was applied to simulate the magnetic field of objects with known susceptibilities. Our Institutional Review Board approved the human subject study and informed consent was obtained from each subject.

All imaging experiments were performed on a 3T MRI system (Magnetom Trio Tim; Siemens Medical Solutions, Erlangen, Germany) using a spoiled 3D multi-echo GRE sequence. Imaging parameters are detailed in Table 1. Agar phantom #1 contained a small cylinder (~1.5 cm diameter and 4.0 cm length) doped with a single concentration of an iron oxide contrast agent (~67.5 ng/ μ L). Agar phantom #2 contained a small cylinder consisting of three sections of different concentrations of iron oxide contrast agent (~22.5 ng/ μ L, 33.8 ng/ μ L, 67.5 ng/ μ L). Both phantoms were imaged three times with the cylinder axis oriented at approximately 0°, 45°, and 90° with respect to B_0 . Healthy volunteers ($n = 5$) were scanned in two positions; with their heads in neutral and chin-down positions. Patients with intracerebral hemorrhages ($n = 5$) were scanned once in a neutral position and images were reviewed by an experienced radiologist.

Numerical Calculation of the Magnetic Field Produced by Material Susceptibility

The magnetic field generated by a given susceptibility distribution in a phantom was calculated in the following manner. The susceptibility distribution geometry of the phantom was defined on the first echo (short TE) magnitude images acquired at each orientation. By convolving the expected susceptibility distribution with the dipole kernel according to the Maxwell's Equations for static magnetism (21,28,29), we obtained the magnetic field relative to B_0 ,

$$\delta(r) = \int_{r' \neq r} \chi(r') \frac{3\cos^2(\theta_{r-r'}) - 1}{4\pi|r' - r|^3} d^3r' = d(r) \otimes \chi(r), \quad [1]$$

where $\delta(r) = (B(r) - B_0)/B_0$ is the susceptibility-induced difference field measured relative to B_0 (relative difference field), $d(r) = (3\cos^2(\theta_r) - 1)/4\pi r^3$ is the dipole kernel, $\chi(r)$ is the susceptibility distribution, r and r' refer to the locations of the observed field and susceptibility source respectively, $\theta_{r-r'}$ is the angle between the vector $r - r'$ and the z -axis. Strictly speaking, the B field in Eq. 1

should be called the magnetic-flux density or magnetic induction along the z -direction. The magnetic field is the B field divided by the permeability ($1 + \chi$), which can be approximated as 1 when dealing with the small susceptibility of biological tissue ($\chi \ll 1$) in Eq. 1. Therefore for simplicity, the B field in MRI is commonly called the magnetic field. The convolution in Eq. 1 was executed efficiently as a multiplication in the Fourier domain by using the Fast Fourier Transform (30).

Construction of Quantitative Susceptibility Maps from Gradient Echo MRI Data

The phase images were first extracted from the complex MRI data, unwrapped using a magnitude image guided algorithm (31), and then a weighted linear fitting of the phase images was performed on a voxel-by-voxel-basis to estimate the susceptibility-induced magnetic field (12). All echoes were used to fit the phase images for human subjects, but only the first three echoes were used for the two iron oxide phantoms due to low signal-to-noise ratio at long TE points. To extract the local fields generated by brain tissues, the background field generated by sources outside the brain region was removed by applying a projection onto dipole fields procedure on the frequency offset map (13). The local field map was then input into a solver with the following cost function for the field-to-source inverse problem (13,23,32):

$$\chi^* = \operatorname{argmin}_{\chi} \|M\nabla\chi\|_1 + \lambda \|W(\delta - d \otimes \chi)\|_2^2. \quad [2]$$

Here ∇ is a 3D gradient operator; M is a binary mask with 0 for voxels of non-trivial gradients in the magnitude image (defined as five times greater than the background noise standard deviation in the magnitude image) and 1 otherwise; W is a weighting set to the SNR of the magnitude image; and λ is the regularization parameter. λ was determined by the discrepancy principle; λ was chosen such that the data term $\|W(\delta - d \otimes \chi)\|_2$ approximately equaled the norm of the noise in $W\delta$, the weighted relative difference field.

Quantitative Data Analysis

Magnitude intensity values, magnetic field values, and susceptibility values were measured manually in regions of interests on magnitude, field, and QSM images for

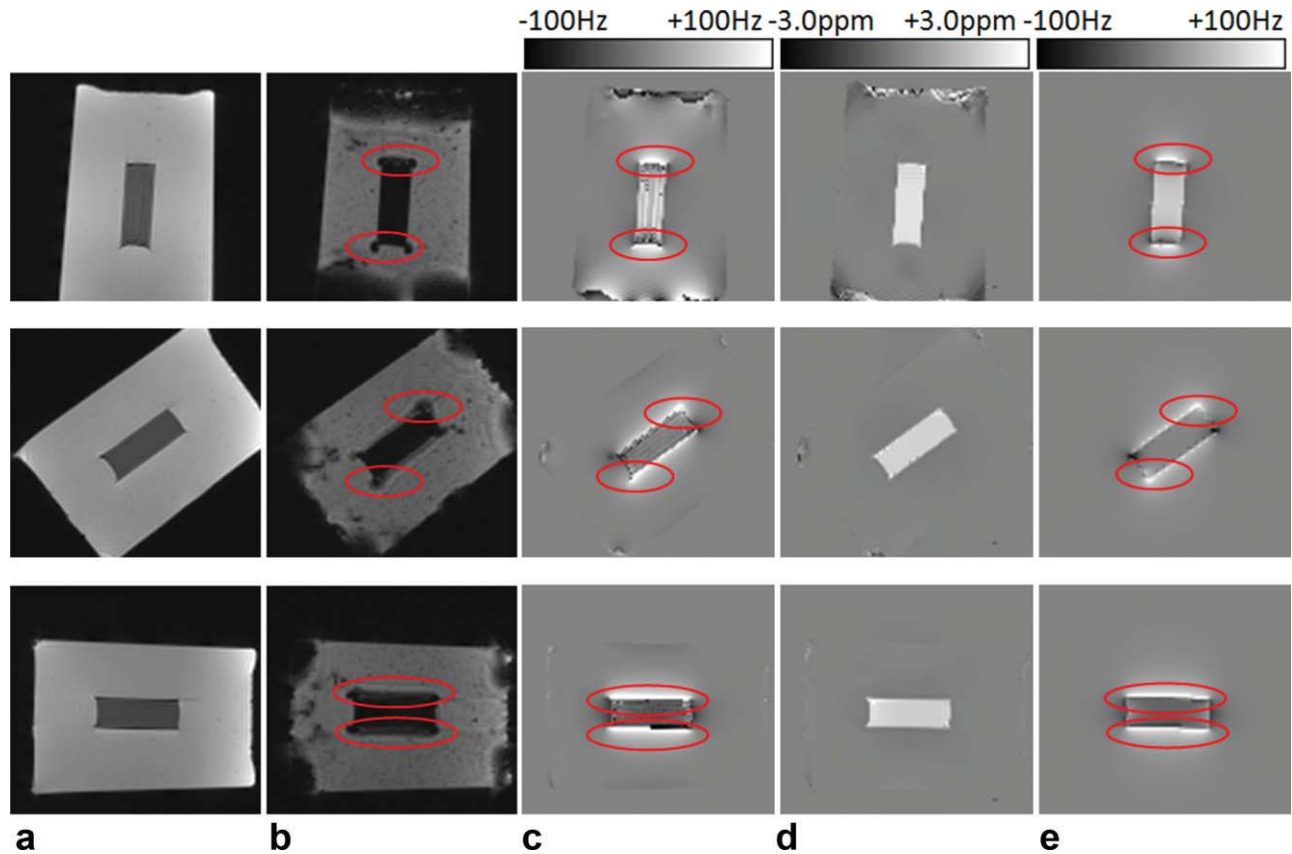


FIG. 1. Coronal images of phantom #1 in three orientations with its cylindrical axis aligned approximately parallel to B_0 (top), at 45° with respect to B_0 (middle) and orthogonal to B_0 (bottom). B_0 is along the vertical axis here. (a,b) GRE magnitude images at TE = 4 ms and 36 ms, respectively, (c) measured field map, (d) QSM, and (e) calculated field map. The calculated field (e) of the cylinder doped with iron oxide contrast agents agrees very well with the measured field (c). Blooming artifacts appear at locations with strong field variation (red ellipses), typically interfaces perpendicular to B_0 . [Color figure can be viewed in the online issue, which is available at wileyonlinelibrary.com.]

both phantoms and human subjects using the MRIcro image viewer (Version 1.40; <http://www.cabiatl.com/mri-cro/>). Field and QSM measurements in phantoms were performed on ROIs of 30 voxels in the centers of regions doped with iron oxide as identified in the magnitude images of the shortest TE and were correlated with the known iron concentrations. Summary statistics (mean \pm standard deviation over ROI) were reported. Field and QSM measurements on the inferior sagittal sinus in healthy subjects were performed using ROIs of 15 voxels, and paired t -tests were performed to assess the statistical differences between the two orientations.

RESULTS

The experimental measurements and the numerical calculations for phantom #1 are shown in Fig. 1. T_2^* magnitude image contrast changed markedly as echo time TE increased. Strong hypointense blooming artifacts appeared at the superior and inferior surfaces of the cylinder perpendicular to B_0 in the magnitude image of TE = 36 ms (Fig. 1b) and were associated with strong magnetic field variations in space, as identified by red ellipses in Fig. 1b and c. The MRI measured fields were consistent with the fields calculated from Eq. 1 using the susceptibility source geometry defined by the TE = 4

ms magnitude images (Fig. 1c and e). The blooming artifacts in the TE = 36 ms magnitude image changed markedly when reorienting the principal axis of the cylinder from parallel to B_0 (top in Fig. 1) to perpendicular to B_0 (bottom in Fig. 1). (The images in the three rows of Fig. 1 were from similar but not identical sections of the phantom due to the repositioning between acquisitions). When the agar cylinder axis was perpendicular to B_0 (bottom row in Fig. 1), the area of blooming artifacts were the largest (Fig. 1b, bottom vs. top and middle).

The field values in the central region of the cylinder were strongly dependent on orientation. The field values were positive (58 ± 18 Hz) when the agar cylindrical axis was at 0° (parallel to B_0) (top in Figs. 1c and e), but the field values were close to zero (-3 ± 9 Hz) and negative (-40 ± 19 Hz) when the cylindrical axis was at 45° and 90° , respectively (middle and bottom in Figs. 1c and e). Compared to the strongly orientation-dependent hypointense blooming artifacts in the TE = 36 ms magnitude images and in the field maps, the estimated quantitative susceptibility maps were approximately the same for the three orientations ($\chi = 1.74 \pm 0.09$, 1.66 ± 0.21 , and 1.77 ± 0.20 ppm, respectively, for the 0° , 45° , and 90° orientations of the cylinder axis) (Fig. 1d).

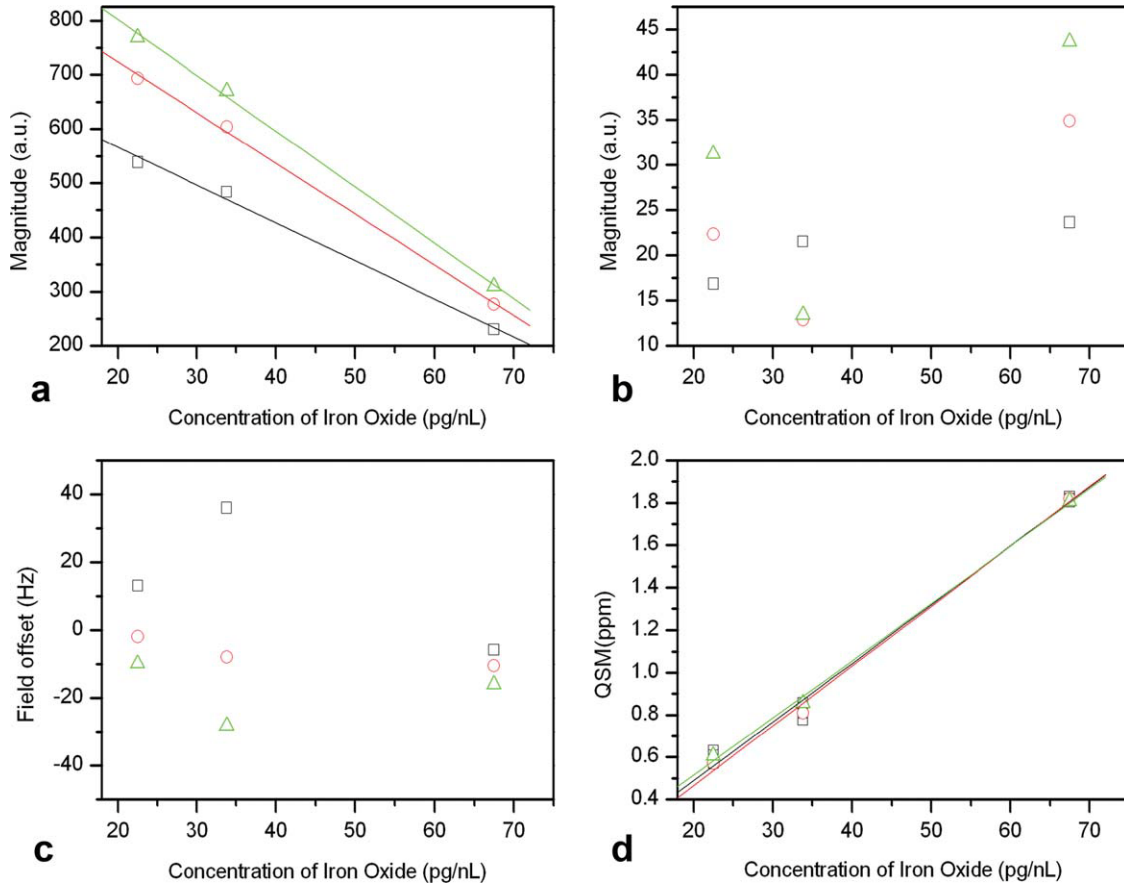


FIG. 2. Correlations between concentrations of iron oxide contrast agents and average magnitude (a,b for TE = 4.2 ms and 33.6 ms, respectively), field (c) and QSM (d) values. The three orientations are (1) approximately parallel to B_0 (box), (2) at an angle of 45° with respect to B_0 (circle) and (3) orthogonal to B_0 (triangle). [Color figure can be viewed in the online issue, which is available at wileyonlinelibrary.com.]

Results from phantom #2 are similar to those from phantom #1. There were strong field variations around the agar layer with the highest concentration of iron oxide. The hypointense blooming artifacts in the TE = 33.6 ms magnitude image changed markedly when the principle axis of the cylinder was repositioned from parallel to B_0 to perpendicular to B_0 . The calculated susceptibility values were approximately the same for the three orientations. There were poor correlations between iron concentrations and field values ($R^2 = 0.08$, Fig. 2c) and between iron concentrations and noisy magnitude hypointensities at TE = 33.6 ms ($R^2 = 0.36$, Fig. 2b). There was a good linear correlation between iron concentrations and magnitude hypointensities at TE = 4.2 ms ($R^2 = 0.84$, Fig. 2a) but the slope and intercept changed with orientation (slope from -7 to -10 , intercept from 706 to 1008). Finally, there was a strong linear correlation between iron concentrations and QSM estimated susceptibilities ($R^2 = 0.99$, Fig. 2d) with the slope and intercept similar for all orientations (slope 0.0277 ± 0.0006 , intercept -0.06 ± 0.04).

The orientation dependence of susceptibility effects was also observed in all human imaging. For example, the field values of the inferior sagittal sinus (red ellipses in Fig. 3) changed substantially between the two head orientations (-9 ± 3 Hz and 15 ± 3 Hz for the two orien-

tations in Fig. 3), but its QSM values remained approximately the same for the two head orientations ($\chi = 0.38 \pm 0.12$ and 0.43 ± 0.09 for the two orientations in Fig. 3). The mean field values of the inferior sagittal sinus from five healthy human subjects were -8 ± 2 Hz and 11 ± 3 Hz for the two orientations, which were significantly different ($p = 0.004$). The mean susceptibilities of the inferior sagittal sinus from five healthy human subjects were 0.39 ± 0.05 and 0.38 ± 0.08 for the two orientations, with no significant difference ($p = 0.67$).

While it was not possible to image hemorrhagic patients with two head orientations, strong blooming artifacts were observed in the superior and inferior aspects of the hemorrhage (red circles in Fig. 4e), compared to the quantitative susceptibility maps (Fig. 4d). The magnetic field in the center of the hemorrhage changed with the shape of hemorrhage. The field value in the center of a hemorrhage was positive (~ 9.7 Hz) when the longest axis of a hemorrhage was approximately parallel to B_0 (top in Fig. 4c), and the field value was negative (approximately -21.9 Hz) when the longest axis of a hemorrhage was approximately perpendicular to B_0 (bottom in Fig. 4c). This sign dependence of the field value of a hemorrhage on its long axis orientation was consistent with that of the iron oxide doped cylinder in phantom #1.

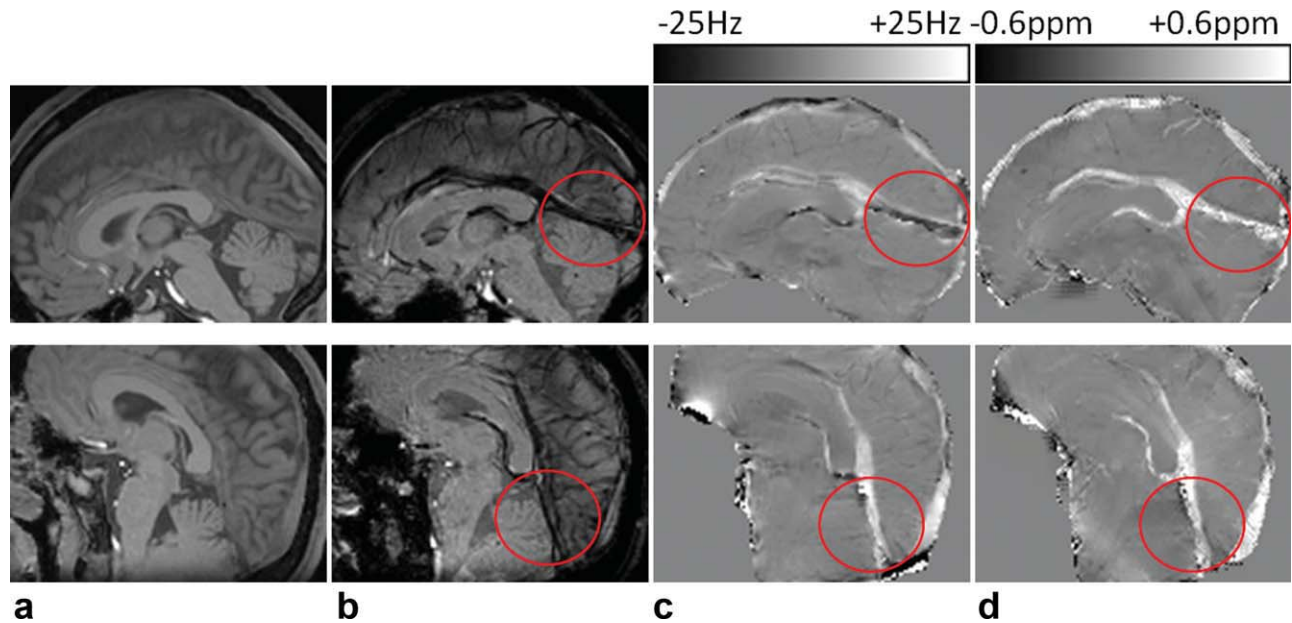


FIG. 3. Images from a healthy subject's brain in the sagittal view with the head at neutral (top) and tilted (bottom) orientations (B_0 is along the vertical axis). (a,b) GRE magnitude images at TE = 3.3 ms and 26.4 ms, respectively, (c) field, and (d) QSM. The inferior sagittal sinus changes its appearance in the magnitude and field images when the orientation with respect to B_0 changes (red ellipses in b,c), but remains consistently paramagnetic independent of orientation in QSM (d).

DISCUSSION

Our data demonstrates that the blooming artifacts in GRE magnitude and phase images occur near the surfaces of the object (susceptibility edges) that are perpendicular to B_0 . These object-orientation dependent susceptibility effects are caused by the local magnetic field that is a convolution of the dipole kernel with all (both local and nonlocal) susceptibility sources within the scanner. The blooming artifacts can be reduced by the dipole deconvolution as is performed in quantitative susceptibility mapping (QSM).

It is known from the Maxwell's Equations for static magnetism that the strong susceptibility-induced fields occur

near the susceptibility interfaces perpendicular to B_0 (28). This explains the observed pattern of blooming artifacts caused by susceptibility inhomogeneities. The induced magnetic field localized along surfaces perpendicular to B_0 causes intravoxel dephasing or T_2^* hypointense blooming artifacts. Change in the surface orientation alters the field distribution and consequently in the blooming artifacts in GRE magnitude and phase data. This analysis based on the Maxwell's Equation may be applied to investigate the orientation effects of structured materials like fibers (25).

There is a substantial difference in the appearances between the local magnetic field and the tissue

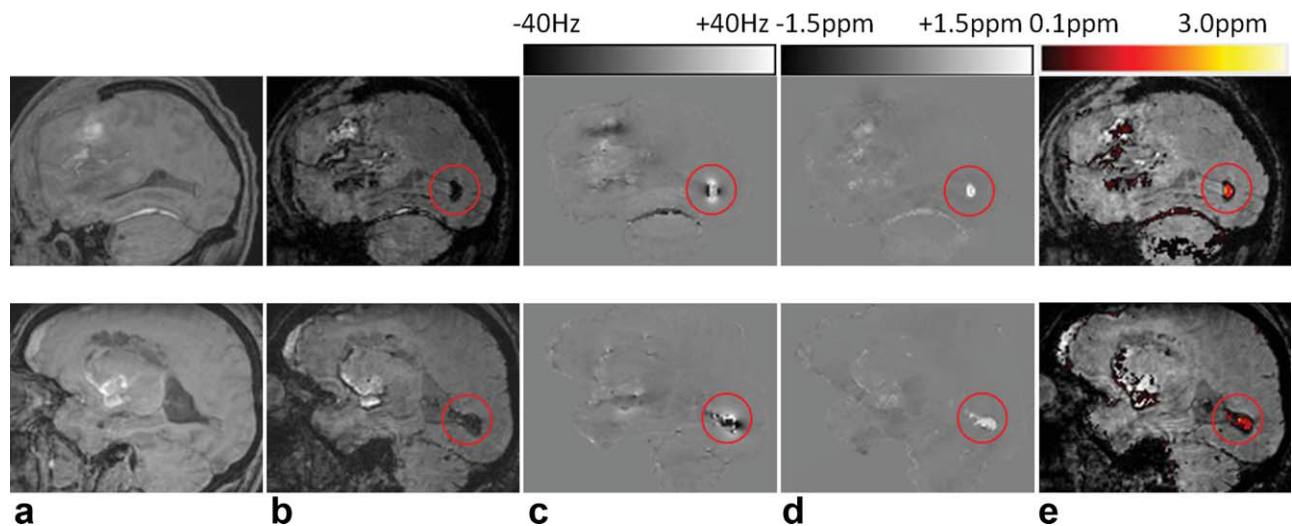


FIG. 4. Sagittal images of the brain of two patients. (a,b) GRE magnitude image at TE = 3.3 ms and 26.4 ms respectively, (c) field, (d) QSM, and (e) QSM with pseudo-color overlaid on the magnitude image at TE = 26.4 ms to show blooming artifacts. The hemorrhages are indicated by the red circles.

susceptibility inducing this field. As demonstrated in Fig. 1c and e, the magnetic field varies widely through the section of approximately uniform susceptibilities. This difference is expected from the Maxwell's Equation, Eq. 1, which indicates that the magnetic field is equal to the convolution of the dipole kernel with the susceptibility map. The dipole kernel makes the field map inhomogeneous even where the underlying material is homogeneous, as seen in Fig. 1c. In special situations when there is a large region of uniform susceptibility, the field at the center of the region may be proportional to the susceptibility. However, this proportionality coefficient changes with the object orientation (see the cylinder center in the top, middle and bottom of Fig. 1c and e) and changes with the shape of the region (see shape differences between Fig. 1c and 4c). High-field MRI has been reported to offer insightful investigation into the biophysical mechanism of phase contrast in GRE (7,24). One should be aware of the difference between non-local phase and local tissue property when the phase in GRE is used to characterize tissue such as brain iron (33), as the phase value (the extracted field value after unwrapping and TE division, to be precise) may provide erroneous iron measurements (34).

Fundamentally, removing blooming artifacts in GRE data requires deconvolution of the dipole kernel. The need and challenge of the dipole deconvolution have been well recognized in literature (21,35). Dipole deconvolution can be regarded as a division by the dipole kernel in k -space. The zeroes in the dipole kernel (and in its derivatives at large k_z s) and the noise make the dipole deconvolution ill-posed, i.e., many possible susceptibility solutions exist that induce the same field as measured from the phase data. Additional prior information is required to select a physically meaningful solution, and error in this prior information model propagates into the selected solution. The prior information used in Eq. 2 is that the susceptibility map should have same structural consistency (such as sharing the same edges) with the magnitude images that naturally coexist with the phase images in GRE data. Because most possible dipole inverse solutions contain artifacts streaking away from susceptibility sources, the prior in Eq. 2 offers a fairly accurate susceptibility solution of minimal streaking artifacts as quantitatively confirmed in experimental validation (13,23). Our phantom data here clearly demonstrate that this quantitative susceptibility mapping method effectively reduces the blooming artifacts.

QSM can be used to provide a more accurate definition of the geometry of high susceptibility tissues, such as hemorrhages with deposits of hemosiderin that are known to have very high susceptibility. GRE MRI is known to be as accurate as CT in detecting acute hemorrhages and more accurate than CT in detecting chronic intracerebral hemorrhages (36). However, blooming artifacts in the T_2^* hypointensity of the magnitude images of GRE depend on the hemorrhage orientation and imaging parameters including the main field strength, voxel size, and echo time. Consequently, it is difficult to measure the actual hematoma volume (37), which is one of the important clinical indices used in the current intracerebral hemorrhage management. By reducing blooming

artifacts, QSM may enable a universal standard for measuring hematoma volume in GRE MRI.

QSM may be used to quantify iron deposition, as validated in Fig. 2d in the phantom experiment and indicated in Fig. 4d for in vivo hemosiderin deposition measurement. QSM may also be used to quantify deoxyhemoglobin as indicated in Fig. 3d where the voxel value of a vein is its deoxyhemoglobin concentration times the molar susceptibility of deoxyhemoglobin. In our human subject QSM, we have noted high susceptibility values in the basal ganglia, substantia nigra, and red nuclei, which may result from ferritin depositions in these regions. We have also noted conspicuous negative-susceptibility values associated with calcium depositions in the ventricles. These observations suggest that, when the magnetic biomarker (the dominant susceptibility contributor, such as iron and calcium) of a tissue is known, QSM can be used to quantify the tissue magnetic biomarker.

QSM is a recently developed field-to-source inversion technique for quantitatively mapping tissue magnetic property. The solver for the nonlinear convex problem of Eq. 2 may be optimized using parallel computing for fast convergence. The formulation of Eq. 2 may be improved for precise account of noise in the detected signal. The current simple binary mask in Eq. 2 works surprisingly well, which may be explained as follows. The dipole convolution kernel is globally applied in the forward problem and the dipole deconvolution kernel is also globally applied in the inverse problem. The deconvolution kernel is tuned well by the minimization of Eq. 2 for selecting the susceptibility structures with strong edges in the T_2^* magnitude images. Such a tuned kernel for deconvolution also works well for other susceptibility structures with little contrast in the T_2^* magnitude images. Therefore, the global nature of the dipole deconvolution does not require knowledge of all structures in the image volume to select the physically meaningful solution for susceptibility. This point may warrant rigorous mathematical justification in future work. Experimentally, the structure binary mask in Eq. 2 may be optimized with the structural information from all available images including the phase images, T_1 and T_2 weighted images, in addition to the T_2^* magnitude images.

In summary, strong blooming artifacts in the magnitude and phase images of GRE data appear near the susceptibility interfaces that are orthogonal to the main field of the MRI system. These orientation-dependent non-local susceptibility effects can be explained by the Maxwell's Equations for static magnetism: the susceptibility-induced magnetic field is a convolution of the dipole kernel with all tissue susceptibility sources including non-local ones. Dipole deconvolution in quantitative susceptibility mapping can reduce the blooming artifacts and depict true local tissue magnetic properties.

REFERENCES

1. Frahm J, Haase A, Matthaei D. Rapid NMR imaging of dynamic processes using the FLASH technique. *Magn Reson Med* 1986;3:321-327.
2. Bernstein MA, King KF, Zhou XJ. *Handbook of MRI pulse sequences*: San Diego, CA: Elsevier Academic Press; 2004.
3. Haacke EM, Xu Y, Cheng YC, Reichenbach JR. Susceptibility weighted imaging (SWI). *Magn Reson Med* 2004;52:612-618.

4. Haacke EM, Reichenbach JR, editors. Susceptibility weighted imaging in MRI: basic concepts and clinical applications. Hoboken, NJ: Wiley-Blackwell; 2011.
5. de Crespigny AJ, Roberts TP, Kucharczyk J, Moseley ME. Improved sensitivity to magnetic susceptibility contrast. *Magn Reson Med* 1993;30:135–137.
6. Duyn JH. Study of brain anatomy with high-field MRI: recent progress. *Magn Reson Imaging* 2010;28:1210–1215.
7. Duyn JH, van Gelderen P, Li TQ, de Zwart JA, Koretsky AP, Fukunaga M. High-field MRI of brain cortical substructure based on signal phase. *Proc Natl Acad Sci USA* 2007;104:11796–11801.
8. Nandigam RN, Viswanathan A, Delgado P, Skehan ME, Smith EE, Rosand J, Greenberg SM, Dickerson BC. MR imaging detection of cerebral microbleeds: Effect of susceptibility-weighted imaging, section thickness, and field strength. *Am J Neuroradiol* 2009;30:338–343.
9. Vernooij MW, Ikram MA, Wielopolski PA, Krestin GP, Breteler MM, van der Lugt A. Cerebral microbleeds: accelerated 3D T2*-weighted GRE MR imaging versus conventional 2D T2*-weighted GRE MR imaging for detection. *Radiology* 2008;248:272–277.
10. Greenberg SM, Vernooij MW, Cordonnier C, Viswanathan A, Al-Shahi Salman R, Warach S, Launer LJ, Van Buchem MA, Breteler MM. Cerebral microbleeds: A guide to detection and interpretation. *Lancet Neurol* 2009;8:165–174.
11. Schafer A, Wharton S, Gowland P, Bowtell R. Using magnetic field simulation to study susceptibility-related phase contrast in gradient echo MRI. *Neuroimage* 2009;48:126–137.
12. de Rochefort L, Brown R, Prince MR, Wang Y. Quantitative MR susceptibility mapping using piece-wise constant regularized inversion of the magnetic field. *Magn Reson Med* 2008;60:1003–1009.
13. de Rochefort L, Liu T, Kressler B, Liu J, Spincemaille P, Lebon V, Wu J, Wang Y. Quantitative susceptibility map reconstruction from MR phase data using bayesian regularization: Validation and application to brain imaging. *Magn Reson Med* 2010;63:194–206.
14. Li W, Wu B, Liu C. Quantitative susceptibility mapping of human brain reflects spatial variation in tissue composition. *Neuroimage*. 2011;55:1645–1656.
15. Schweser F, Deistung A, Lehr BW, Reichenbach JR. Differentiation between diamagnetic and paramagnetic cerebral lesions based on magnetic susceptibility mapping. *Med Phys* 2010;37:5165–5178.
16. Shmueli K, de Zwart JA, van Gelderen P, Li TQ, Dodd SJ, Duyn JH. Magnetic susceptibility mapping of brain tissue in vivo using MRI phase data. *Magn Reson Med* 2009;62:1510–1522.
17. Wharton S, Bowtell R. Whole-brain susceptibility mapping at high field: a comparison of multiple- and single-orientation methods. *Neuroimage* 2010;53:515–525.
18. Wharton S, Schafer A, Bowtell R. Susceptibility mapping in the human brain using threshold-based k-space division. *Magn Reson Med* 2010;63:1292–1304.
19. Kressler B, de Rochefort L, Liu T, Spincemaille P, Jiang Q, Wang Y. Nonlinear regularization for per voxel estimation of magnetic susceptibility distributions from MRI field maps. *IEEE Trans Med Imaging* 2010;29:273–281.
20. Liu T, Spincemaille P, de Rochefort L, Kressler B, Wang Y. Calculation of susceptibility through multiple orientation sampling (COSMOS): A method for conditioning the inverse problem from measured magnetic field map to susceptibility source image in MRI. *Magn Reson Med* 2009;61:196–204.
21. Li L, Leigh JS. Quantifying arbitrary magnetic susceptibility distributions with MR. *Magn Reson Med* 2004;51:1077–1082.
22. Liu C. Susceptibility tensor imaging. *Magn Reson Med* 2010;63:1471–1477.
23. Liu J, Liu T, de Rochefort L, Ledoux J, Khalidov I, Chen W, Tsiouris AJ, Wisnieff C, Spincemaille P, Prince MR, Wang Y. Morphology enabled dipole inversion for quantitative susceptibility mapping using structural consistency between the magnitude image and the susceptibility map. *Neuroimage* 2011 doi: 10.1016/j.neuroimage.2011.08.082.
24. He X, Yablonskiy DA. Biophysical mechanisms of phase contrast in gradient echo MRI. *Proc Natl Acad Sci USA* 2009;106:13558–13563.
25. Lee J, van Gelderen P, Kuo LW, Merkle H, Silva AC, Duyn JH. T(2)*-based fiber orientation mapping. *Neuroimage* 2011;57:225–234.
26. Lee J, Shmueli K, Fukunaga M, van Gelderen P, Merkle H, Silva AC, Duyn JH. Sensitivity of MRI resonance frequency to the orientation of brain tissue microstructure. *Proc Natl Acad Sci USA* 2010;107:5130–5135.
27. Walsh A, Wieler M, Martin W, Wilman AH. Susceptibility phase imaging of the basal ganglia: Effects of phase filtering, slice orientation and ROI selection with comparison to T2* mapping. In: Proceedings of the 18th Annual Meeting of ISMRM, Stockholm, Sweden.2010.
28. Jackson JD. Classical electrodynamics, 3rd ed. New York: John Wiley and Sons, Inc.; 1999.
29. de Rochefort L, Nguyen T, Brown R, Spincemaille P, Choi G, Weinsaft J, Prince MR, Wang Y. In vivo quantification of contrast agent concentration using the induced magnetic field for time-resolved arterial input function measurement with MRI. *Med Phys* 2008;35:5328–5339.
30. Salomir R, De Senneville BD, Moonen CTW. A fast calculation method for magnetic field inhomogeneity due to an arbitrary distribution of bulk susceptibility. *Concept Magn Reson B* 2003;19:26–34.
31. Cusack R, Papadakis N. New robust 3-D phase unwrapping algorithms: Application to magnetic field mapping and undistorting echoplanar images. *Neuroimage* 2002;16:754–764.
32. Liu T, Liu J, de Rochefort L, Spincemaille P, Khalidov I, Ledoux JR, Wang Y. Morphology enabled dipole inversion (MEDI) from a single-angle acquisition: Comparison with COSMOS in human brain imaging. *Magn Reson Med* 2011;66:777–783.
33. Haacke EM, Ayaz M, Khan A, Manova ES, Krishnamurthy B, Gollapalli L, Ciulla C, Kim I, Petersen F, Kirsch W. Establishing a baseline phase behavior in magnetic resonance imaging to determine normal vs. abnormal iron content in the brain. *J Magn Reson Imaging* 2007; 26:256–264.
34. Yao B, Li TQ, Gelderen P, Shmueli K, de Zwart JA, Duyn JH. Susceptibility contrast in high field MRI of human brain as a function of tissue iron content. *Neuroimage* 2009;44:1259–1266.
35. Haacke EM, Cheng NY, House MJ, Liu Q, Neelavalli J, Ogg RJ, Khan A, Ayaz M, Kirsch W, Obenaus A. Imaging iron stores in the brain using magnetic resonance imaging. *Magn Reson Imaging* 2005;23:1–25.
36. Kidwell CS, Chalela JA, Saver JL, Starkman S, Hill MD, Demchuk AM, Butman JA, Patronas N, Alger JR, Latour LL, Luby ML, Baird AE, Leary MC, Tremwel M, Ovbiagele B, Fredieu A, Suzuki S, Villablanca JP, Davis S, Dunn B, Todd JW, Ezzeddine MA, Haymore J, Lynch JK, Davis L, Warach S. Comparison of MRI and CT for detection of acute intracerebral hemorrhage. *JAMA* 2004;292:1823–1830.
37. Burgess RE, Warach S, Schaewe TJ, Copenhaver BR, Alger JR, Vespa P, Martin N, Saver JL, Kidwell CS. Development and validation of a simple conversion model for comparison of intracerebral hemorrhage volumes measured on CT and gradient recalled echo MRI. *Stroke* 2008;39:2017–2020.